

Two-dimensional non-Hermitian Su-Schrieffer-Heeger Model

Udai Prakash Tyagi and Partha Goswami

Email of the first author: uptyagi@yahoo.co.in

Email of the corresponding author: physicsgoswami@gmail.com

Abstract

A particle-hole symmetry protected 2D non-Hermitian Su-Schrieffer-Heeger (SSH) model is investigated. This version differs from the usual Hermitian version by the inclusion of gain and/or loss terms which are represented by complex on-site potentials. The exceptional points occur, when the dimensionless potential magnitude and the hopping amplitudes become close to unity, leading to the coalescence of eigenvalues and nontrivial eigenvector degeneracies. Furthermore, the vectored Zak phase quantization has been obtained and a topoelectric RLC circuit has been analysed. If realized experimentally (in photonic and acoustic crystals), the quantization is expected to lead to an extended bulk-boundary correspondence.

1. Introduction

The topological insulators (TIs) and their higher order variants (HOTI) [1-4] are materials that are insulating in the bulk but have topologically protected, conducting surface states. The protection requires time-reversal symmetry to be preserved. The energy dispersion relation of these insulators exhibits a Dirac cone shape. In this communication, we investigate a two-dimensional Su-Schrieffer-Heeger (2DSSH) model $H_{SSH,2D}$ (see Figure 1 and Eq. (1)). This is an extended version of the simplest models of topology referred to as 1 D SSH model [5]. In Figure 1, the numerals 1,2,3, and 4 correspond to the lattice sites A, B, C, and D, respectively, of a square lattice with lattice constant 'a'. While the symbols u and t_1 stand for the hopping parameters along x - direction, the symbols v and t_2 are those along y - direction. The imaginary staggered potentials (ISP) on (A, B) and (C, D), respectively, are $(i\gamma, -i\gamma)$ and $(-i\gamma, i\gamma)$ in the Hamiltonian $H_{SSH,2D}$. These are the non-Hermitian strengths in the unit cell. We may also have the case which corresponds to ISP on (1, 2) and (3, 4), respectively, are $\{(i\gamma_1, -i\gamma_1)$ and $(i\gamma_2, -i\gamma_2)\}$ where $\gamma_1 \neq \gamma_2$. We may denote the Hamiltonian in this case as $H'_{SSH,2D}$. These imaginary staggered potentials are the additional terms involved in the matrix form of the Hamiltonian to be presented below. We choose the wavenumber $\mathbf{k} = (k_x, k_y)$ to take on values from the first Brillouin zone (BZ) in the Hamiltonian $H_{SSH,2D}(\mathbf{k} = (k_x, k_y))$ in the \mathbf{k} -space. The Hamiltonian $H_{SSH,2D}(k_x, k_y)$ will be shown to be PT -symmetric [6] (eigenvalues are real) if $u = t_1$ in a limited region of two-dimensional BZ. For $u \neq t_1$ and elsewhere in BZ, the Hamiltonian has complex eigenvalues, and the system enters a broken PT -symmetric phase. A detailed discussion on the symmetries associated with $H_{SSH,2D}(k_x, k_y)$ is given in section 2. As we shall see that the time reversal symmetry (TRS) is not preserved in some cases. The reason being the hopping parameters along x - and y - directions in $H_{SSH,2D}(k_x, k_y)$ may not be equal and the presence of the imaginary staggered potentials. An important question "Can we create a topological insulating and conducting phases solely from the gain and loss control?" arises in the context of the present communication. Our graphical representations in Figure 2 show that regulatable gain/loss

parameter (γ) transforms the system from an insulator to a conductor when its numerical value is decreased.

Furthermore, in general, the bulk-boundary correspondence is the central theme in topologically non-trivial systems. The topological invariant for such system-models is their Zak phase [7,8]. This phase predicts the existence or absence of edge states in various cases

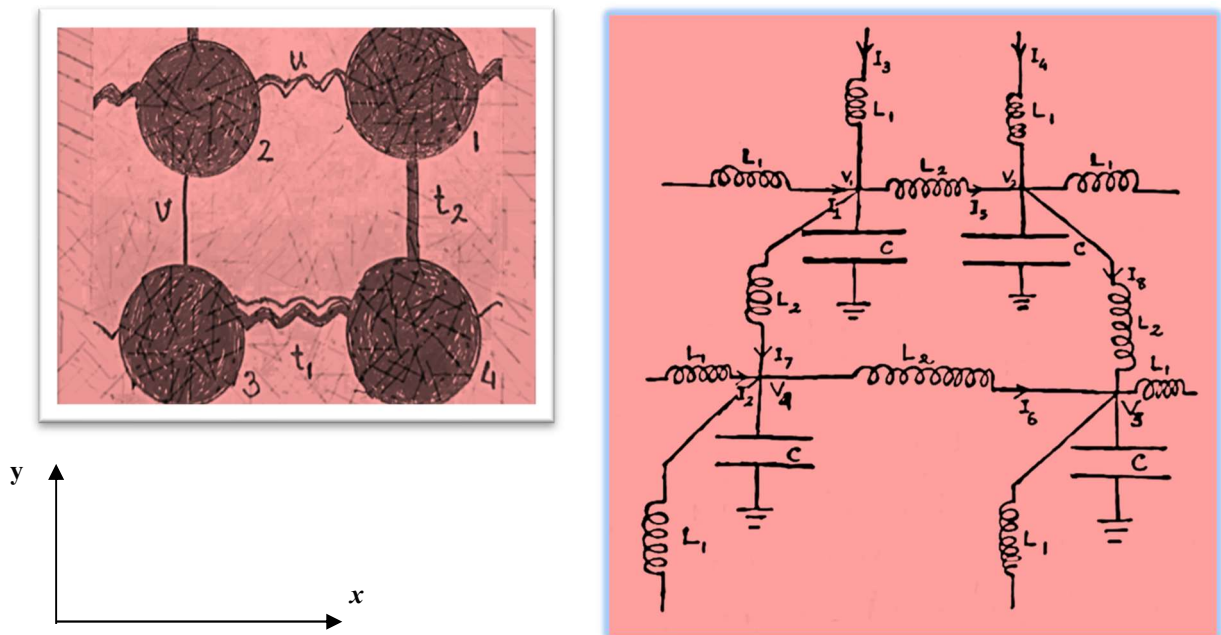


Figure 1. (a) A pictorial representation of two-dimensional non-Hermitian Su-Schrieffer-Heeger (2DSSH) model. Here, 1,2,3, and 4 correspond to the lattice sites A, B, C, and D, respectively, of the model lattice. While the symbols u and t_1 stand for the hopping parameters along x - direction, the symbols v and t_2 are those along y - direction. The imaginary staggered potentials on (A, B) and (C, D), respectively, are $(i\gamma, -i\gamma)$ and $(-i\gamma, i\gamma)$. (b) A topoletric RLC circuit with the four-site unit cell. The node voltages $V_1, V_2, V_3,$ and V_4 correspond to the four sites (nodes) 1,2,3, and 4, respectively. The resistors(R) are assumed (not shown) to be in parallel with the capacitors (C).

[7]. The phase is measured in modulo (2π) . Thus, the phase is quantized to $n\pi$ where $n = 0,1$. The quantization upholds the bulk-boundary correspondence. The phase, which is essentially an integral in 1D (but could be extended for the 2D case as shown in section 3), is defined as $\phi = \oint dk A(k)$ where the integral is over BZ and $A(k)$ is the Berry connection given by $A(k) = i\langle\psi(k)|\partial_k|\psi(k)\rangle$. The state $|\psi(k)\rangle$ gives the periodic part of Bloch wavefunction. When the phase takes on the value of π , edge states appear, and they are topologically protected. We calculate the vectored Zak phase in section 3 for our 2D system leading to the bulk-boundary correspondence in certain parameter window.

As a warm-up activity and a good starting point, we first discuss in brief the 1 D SSH model H_{SSH} [9].It is a special case of $H_{SSH,2D}$ [10, 11]. The model Hamiltonian H_{SSH} yields the bulk-boundary correspondence when the chiral symmetry is preserved. The edge states correspond

to bipartite (tight binding) Hamiltonian for a molecular chain, viz. $H_{SSH} = \sum_n [v |n, B\rangle \langle n, A| + w |n+1, A\rangle \langle n, B|] + h.c.$, where n labels the unit cell and A and B are the different sublattices with hopping parameters v and w between them. Here $|n, A\rangle$ ($|n, B\rangle$), with $n \in \{1, 2, \dots, N\}$ denotes the state of the chain where the electron is on unit cell n , in the site on sublattice A (B), and h.c. stands for Hermitian Conjugate e.g., h.c. of $|n, B\rangle \langle n, A|$ is $\langle n, A| \langle n, B|$. The Hamiltonian may also be written in terms of the creation (a_n^\dagger (b_n^\dagger)) and annihilation operators (a_n (b_n)), for the sublattice site indexed ' n ', as $\sum_n [v a_n^\dagger b_n + w b_n^\dagger a_{n+1} + h.c.]$. The non-Hermitian variant of it may have additional terms in the Hamiltonian which represent the gain and the loss. The corresponding k -space Hamiltonian matrix, without the gain/loss term, may be written out as $H_{SSH}(k) = (v + t \cos(ak_x)) \sigma_x + (-w \sin(ak_x)) \sigma_y$ where σ_j 's are Pauli matrices. As long as the hopping amplitudes are staggered ($v \neq w$), there is an energy gap separating the lower, filled band, from the upper, empty band. However, when $v = w$, the SSH model describes a conductor. We shall discuss an analogous situation in section 4 with the Hamiltonian $H_{SSH,2D}(k_x, k_y)$. Apart from the translation symmetry and the time reversal symmetry, the other symmetries in $H_{SSH}(k)$ are the chiral symmetry, the particle-hole symmetry, and the inversion symmetry. In contrast, the 2D model rectangular lattice considered here comprises of sites located at $\{\mathbf{R}, \mathbf{R} + \Delta R_x \hat{x}, \mathbf{R} + 2\Delta R_x \hat{x}, \dots\}$ in the x -direction and same number of sites located at $\{\mathbf{R}, \mathbf{R} + \Delta R_y \hat{y}, \mathbf{R} + 2\Delta R_y \hat{y}, \dots\}$ in the y -direction. In the absence of ISPs, the 2D model can be described by the following the effective tight binding model (ETB) (cf. Figure 1):

$$H_{SSH,2D} = \sum_{\mathbf{R}} \{ u |\mathbf{R}, A\rangle \langle \mathbf{R}, B| + t_1 |\mathbf{R} + \Delta R_x \hat{x}, B\rangle \langle \mathbf{R}, A| + t_1 |\mathbf{R}, C\rangle \langle \mathbf{R}, D| + u |\mathbf{R} + \Delta R_x \hat{x}, D\rangle \langle \mathbf{R}, C| + v |\mathbf{R}, B\rangle \langle \mathbf{R}, C| + t_2 |\mathbf{R} + \Delta R_y \hat{y}, C\rangle \langle \mathbf{R}, B| + t_2 |\mathbf{R}, D\rangle \langle \mathbf{R}, A| + v |\mathbf{R} + \Delta R_y \hat{y}, A\rangle \langle \mathbf{R}, D| \} + h.c. . \quad (1)$$

The effective tight binding model of a crystal, in fact, is a theoretical model that describes the behavior of the crystal's vibrations in terms of the interaction between its constituent atoms or molecules. In this model, the crystal is treated as a lattice of discrete points, or "sites," each of which represents an atomic or molecular unit. The strength of the interaction between neighboring sites is characterized by a set of parameters, such as the hopping energy. These are $\{u, v, t_1, t_2\}$ in the present problem under investigation. These parameters are typically determined by fitting the model to experimental data or more detailed calculations, and can be used to obtain the energy dispersion relations and density of states for the crystal. The ETB is useful for studying the properties of acoustic crystals and can be used to predict a variety of phenomena, such as band gaps, resonance modes, etc..

The reason for the choice of the non-hermiticity is explained below: The TIs and HOTIs (usually the artificial classical structures) are defined under the Hermitian condition. However, such systems involve intrinsic loss which requires the corresponding Hamiltonian to be non-Hermitian in nature. Besides, a non-Hermitian system usually leads to a large number of novel phenomena absent in Hermitian dispersions. An important one is that, under open boundary

conditions (OBC), the energy spectra of such systems respond to boundary conditions quickly with the corresponding eigenstates pushed towards the system boundaries. In fact, there is an extreme boundary-sensitivity of non-Hermitian topological zero modes. This shifting is referred to as the non-Hermitian skin effect (NHSE) [12–23]. This effect has been studied both experimentally and theoretically [24–32]. For example, Kawabata et al. [12,13] have reported higher-order NHSE. The detailed report of an experimental demonstration of non-Hermiticity-induced HOTI was provided by He Gao et al. [15]. The extensive appeal of the effect is due to its deviation from the Bloch band theory. The effect has its wide range of important applications [32–38], such as non-Hermitian topological sensor [32] and topoelectric circuit (TC) sensor [33], topological funneling of light [38], and so on. We investigate some aspect of TC [29] in this communication (see Figure 1(b)). Another important aspect of non-hermiticity of the Hamiltonian is that it exhibits the exceptional points on which band touching occurs for both real and imaginary parts [39–44]. We also report the outcome of investigation of this issue in this paper.

The paper is organized as follows: We present the 2D SSH model in section 2 and discuss its symmetry properties. We obtain the energy eigenvalues and the corresponding eigenvectors in this section in PT symmetric/ non-symmetric cases. We also show that for our non-Hermitian Hamiltonian case, the exceptional points occur only if the Hamiltonian is PT-symmetric. We calculate the Zak phase in section 3 leading to the bulk-boundary correspondence. In this section, we also investigate a topoelectric RLC circuit as an application of the model presented. We present a discussion in section 4 relating to a case where the hopping amplitudes are staggered in \hat{y} - direction. The paper ends with concluding remarks in section 5.

2. Model and Method

Model

In this section we write down the Hamiltonian introduced in Eq.(1) in momentum space. We will compare this with a TC Hamiltonian as well. In Figure 1, the numerals 1,2,3, and 4 correspond to the lattice sites A, B, C, and D, respectively, of a square lattice with lattice constant ‘ a ’. The Hamiltonian in the absence of ISP, presented above, may also be written slightly differently in terms of the site creation operator $\{a_{R,1}^\dagger, b_{R,2}^\dagger, \dots\}$ and the site annihilation operators $\{a_{R,1}, b_{R,2}, \dots\}$ as

$$\begin{aligned}
H_{SSH,2D} = \sum_{\mathbf{R}} [& u a_{R,1}^\dagger b_{R,2} + u b_{R,2}^\dagger a_{R,1} + t_1 c_{R,3}^\dagger d_{R,4} + t_1 d_{R,4}^\dagger c_{R,3} + v b_{R,2}^\dagger c_{R,3} + v c_{R,3}^\dagger b_{R,2} + \\
& t_2 d_{R,4}^\dagger a_{R,1} + t_2 a_{R,1}^\dagger d_{R,4} + u d_{R,4}^\dagger c_{R+\Delta R_x \hat{x}, 3} + u c_{R+\Delta R_x \hat{x}, 3}^\dagger d_{R,4} + v d_{R+\Delta R_y \hat{y}, 4}^\dagger a_{R,1} + \\
& v a_{R,1}^\dagger d_{R+\Delta R_y \hat{y}, 4} + t_1 b_{R+\Delta R_x \hat{x}, 2}^\dagger a_{R,1} + t_1 a_{R,1}^\dagger b_{R+\Delta R_x \hat{x}, 2} + t_2 b_{R,2}^\dagger c_{R+\Delta R_y \hat{y}, 3} + \\
& t_2 c_{R+\Delta R_y \hat{y}, 3}^\dagger b_{R,2}]. \quad (2)
\end{aligned}$$

The spin degree of freedom is completely absent from the 2DSSH model, since no term in the Hamiltonian acts on spin. Thus, the 2D SSH model describes spin-polarized electrons, and when applying the model to a real physical system, we have to always take two copies of it. The Hamiltonian given by (2) is the same as that in (1). We assume that the periodic boundary

condition $|\mathbf{R} + N\Delta\mathbf{R}, P\rangle = |\mathbf{R}, P\rangle$ for the x - and the y -directions where N is the number of sites in these directions. The Fourier transform $|R_x, P\rangle = N^{-\frac{1}{2}} \sum_k e^{ik_x R_x} |k, P\rangle$ and $|R_y, P\rangle = N^{-\frac{1}{2}} \sum_k e^{ik_y R_y} |k, P\rangle$ eventually yields

$$\begin{aligned}
H_{SSH,2D} = & \\
& \sum_R \sum_k \left\{ \left[\frac{u}{N} |k, A\rangle \langle k, B| + \frac{t_1}{N} \exp(ik_x(R_x + \Delta R_x)) |k, B\rangle \langle k, A| \exp(-ik_x R_x) + \right. \right. \\
& \quad \left. \left. h. c. \right] + \sum_r \sum_k \left\{ \left[\frac{t_1}{N} |k, C\rangle \langle k, D| + \frac{u}{N} \exp(ik_x(R_x + \Delta R_x)) |k, D\rangle \langle k, C| \exp(-ik_x R_x) + \right. \right. \\
& \quad \left. \left. h. c. \right] \right\} + \sum_R \sum_k \left\{ \left[\frac{v}{N} |k, B\rangle \langle k, C| + \frac{t_2}{N} \exp(ik_y(R_y + \Delta R_y)) |k, C\rangle \langle k, B| \exp(-ik_y R_y) + \right. \right. \\
& \quad \left. \left. h. c. \right] + \sum_s \sum_k \left\{ \left[\frac{t_2}{N} |k, D\rangle \langle k, A| + \frac{v}{N} \exp(ik_y(R_y + \Delta R_y)) |k, A\rangle \langle k, D| \exp(-ik_y R_y) + \right. \right. \\
& \quad \left. \left. h. c. \right] \right\}. \tag{3}
\end{aligned}$$

As the space inversion entails $(k_x, k_y) \rightarrow (-k_x, -k_y)$, the Hamiltonian (3) is invariant under the inversion. We make the replacement

$$\{|k, A\rangle, |k, B\rangle, |k, C\rangle, |k, D\rangle\} \rightarrow \{a_k, b_k, c_k, d_k\} \tag{4}$$

below, where $\{a_k, b_k, c_k, d_k\}$ the destruction operators in momentum space. We can then present the Hamiltonian in the basis $(a_k \ b_k \ c_k \ d_k)^T$ as

$$\begin{aligned}
H_{SSH,2D}(k_x, k_y) = & \\
& \begin{pmatrix} \varepsilon_1 & u + t_1 \exp(iak_x) & 0 & t_2 + v \exp(-iak_y) \\ u + t_1 \exp(-iak_x) & \varepsilon_2 & v + t_2 \exp(iak_y) & 0 \\ 0 & v + t_2 \exp(-iak_y) & \varepsilon_2 & t_1 + u \exp(iak_x) \\ t_2 + v \exp(iak_y) & 0 & t_1 + u \exp(-iak_x) & \varepsilon_1 \end{pmatrix} \tag{5}
\end{aligned}$$

Here $\varepsilon_1 = i\gamma - \mu$, $\varepsilon_2 = -i\gamma - \mu$, (u, t_1) and (v, t_2) , respectively, are the hopping parameters along the x - and the y -directions. The symbol μ stands for the chemical potential. The imaginary staggered potentials (ISP) on (A, B) and (C, D), respectively, are $(i\gamma, -i\gamma)$ and $(-i\gamma, i\gamma)$ are introduced additionally to make the Hamiltonian non-Hermitian.

The basis of $su(4)$ corresponds to anti-Hermitian 4×4 -matrices Λ_j with vanishing traces [38]. The generator 4×4 Hermitian matrices λ_j [38] are expressed in terms of Λ_j as $\lambda_j = 2i\Lambda_j$. The basis for the 4×4 matrix in (5) are these λ_j 's that span the Lie algebra of $SU(4)$ group provided we assume no ISP on the sites (C, D) and $\mu = 0$. In that case (5) could be written as

$$H''_{SSH,2D}(\mathbf{k}) = (u + t_1 \cos(ak_x))\lambda_1 - t_1 \sin(ak_x)\lambda_2 + (v + t_2 \cos(ak_y))\lambda_6 + i\gamma\lambda_3 - t_2 \sin(ak_y)\lambda_7 + (t_2 + v \cos(ak_y))\lambda_9 + v \sin(ak_y)\lambda_{10} + (t_1 + u \cos(ak_x))\lambda_{13} - u \sin(ak_x)\lambda_{14}. \quad (6)$$

Furthermore, it may be easily seen that Eq. (5) reduces to 1D-SSH model in the absence of the $H_{SSH,2D}(-k_x, -k_y)$. Upon getting back to the Hamiltonian $H_{SSH,2D}(k_x, k_y)$ we note that it is PT -symmetric [6] (that is, eigenvalues are real) if $u = t_1$ (and $v = t_2$) in a limited region of two-dimensional BZ. For $u \neq t_1$ (and/or $v \neq t_2$) (see Figure 2(e)) and elsewhere in BZ, the Hamiltonian has complex eigenvalues. The Figures 2(g) and 2(h) corroborate the latter. The particle-hole symmetry (PHS) is satisfied by $H_{SSH,2D}(k_x, k_y)$ as $P H_{SSH,2D}^*(k_x, k_y) P^{-1} = -H_{SSH,2D}(-k_x, -k_y)$, where $P = (\sigma_0 \otimes \sigma_z)$. For the Hamiltonian $H'_{SSH,2D}(k)$ also, PHS is unbroken. In the case of $H'_{SSH,2D}(k)$, we have $M H'_{SSH,2D}(k_x, k_y) M^{-1} \neq -H'_{SSH,2D}(k_x, k_y)$, where the chiral mirror symmetry operator $M = \sigma_x \otimes \sigma_z$. Although the chiral mirror symmetry is broken for $H'_{SSH,2D}(k_x, k_y)$, the Hamiltonian $H_{SSH,2D}(k_x, k_y)$ is invariant under this symmetry. The chiral symmetry ($C H(k) C^{-1} = -H(k)$, where $C = \sigma_y \otimes \sigma_y$) is not respected by $H_{SSH,2D}(k)$. Also, the time reversal symmetry (TRS), where $T = i \sigma_0 \otimes \sigma_y K$, and the operator K stands for the complex conjugation) is not preserved ($T H_{SSH,2D}(k_x, k_y) T^{-1} \neq H_{SSH,2D}(-k_x, -k_y)$), as the unequal hopping parameters (v, t_2) along y -direction together with ISP are involved in $H'_{SSH,2D}(k_x, k_y)$ and $H_{SSH,2D}(k_x, k_y)$. However, when $v = t_2$ (and ISP is zero) TRS is unbroken. As we shall see in section 3 that the broken TRS leads to non-zero Berry curvature and the anomalous Nernst effect for $v \neq t_2$. Here, σ_0 and $\sigma_{x,y,z}$, respectively, are the two-by-two identity matrix and Pauli matrices.

Energy eigenvalues

The energy eigenvalues of (5) are given by the expressions $E_1 = \sqrt{(A + \sqrt{J(k_x, k_y)})}$, $E_2 = -\sqrt{(A + \sqrt{J(k_x, k_y)})}$, $E_3 = \sqrt{(A - \sqrt{J(k_x, k_y)})}$ and $E_4 = -\sqrt{(A - \sqrt{J(k_x, k_y)})}$ where $A(k_x, k_y) = |p|^2 + |s|^2 - \gamma^2$, $p = t_2 + v \exp(-iak_y)$, $s = u + t_1 \exp(iak_x)$, and

$$J(k_x, k_y) = 2|p|^2|s|^2 + 2(t_2 + v \cos(ak_y))F_1(k_x, k_y) - 2(v \sin(ak_y))F_2(k_x, k_y) - 4(|p|^2 + |s|^2)\gamma^2 \quad (7)$$

$$F_1(k_x, k_y) \equiv \{uvt_1 + vt_1^2 + t_1^2 t_2 + ut_1 t_2 \cos(ak_y) + t_2 t_1^2 \cos(ak_x + ak_y) + u^2 v \cos(ak_x) + uvt_1 \cos(2ak_x) + t_2 u^2 \cos(ak_x + ak_y) + ut_1 t_2 \cos(2ak_x + ak_y)\}, \quad (8)$$

$$F_2(k_x, k_y) \equiv \{ut_1 t_2 \sin(ak_y) + t_2 t_1^2 \sin(ak_x + ak_y) + u^2 v \sin(ak_x) + uvt_1 \sin(2ak_x) + t_2 u^2 \sin(ak_x + ak_y) + ut_1 t_2 \sin(2ak_x + ak_y)\}. \quad (9)$$

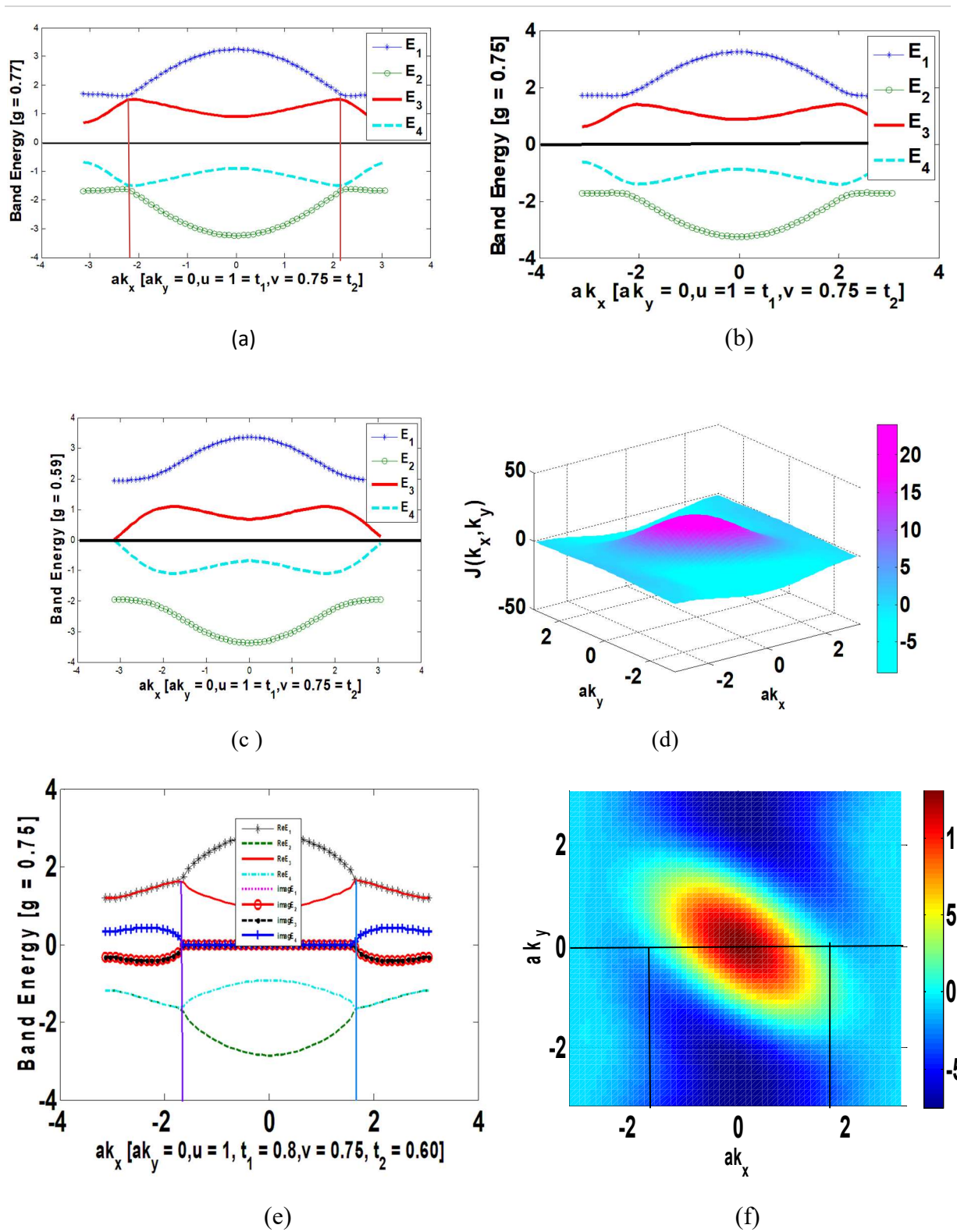
In the Appendix A we have also presented the eigenvectors corresponding to these eigenvalues. We notice that when $J(k_x, k_y) = 0$, the levels (E_1, E_3) are degenerate and equal to $\sqrt{A(k_x, k_y)}$ [similarly (E_2, E_4) are degenerate and equal to $(-\sqrt{A(k_x, k_y)})$]. An exceptional point is a branch point of eigenvalues in the parameter space where not only the eigenvalues but also the eigenstates coalesce. As can be seen in the Appendix A, the eigenvectors $|u^{(1)}(k_x, k_y)\rangle$ and $|u^{(3)}(k_x, k_y)\rangle$, respectively, corresponding to (E_1, E_3) are the same [similarly the eigenvectors $|u^{(2)}(k_x, k_y)\rangle$ and $|u^{(4)}(k_x, k_y)\rangle$, respectively, corresponding to (E_2, E_4) are the same]. The situation is conducive for the occurrence of exceptional point, say, at $k_x = k_{x0}, k_y = k_{y0}$, provided the property of the self-orthogonality $\langle u^{(j)}(k_x = k_{x0}, k_y = k_{y0}) | u^{(j)}(k_x = k_{x0}, k_y = k_{y0}) \rangle = 0$ [45,46] is achieved. It may be emphasized that that self-orthogonality can never occur for an eigenstate of a Hermitian Hamiltonian within the Hilbert space, because the Hermitian conjugate of a right eigenvector in the Hilbert space is the same as the left eigenvector, and by definition a state vector in the Hilbert space has a non-vanishing finite norm.

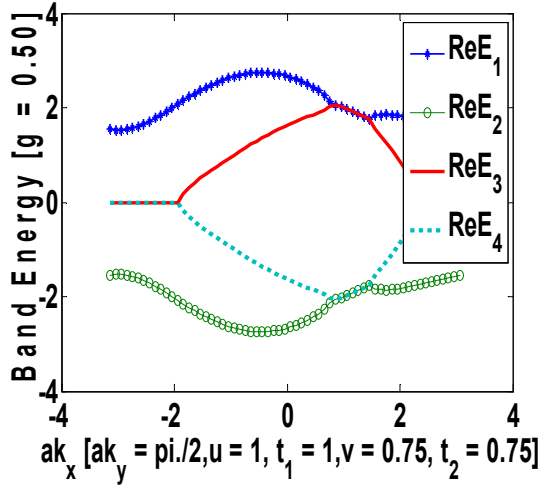
We have shown in the Appendix A that the eigenstates linked to the eigenvalues of (3) could be written down in a general manner as

$$|u^{(j)}(k_x, k_y)\rangle = \frac{1}{N_{j0}^{1/2}} \begin{pmatrix} \psi_1^j(k_x, k_y) \\ \psi_2^j(k_x, k_y) \\ \psi_3^j(k_x, k_y) \\ \psi_4^j(k_x, k_y) \end{pmatrix}, j=1, 2, 3, 4, \quad (10)$$

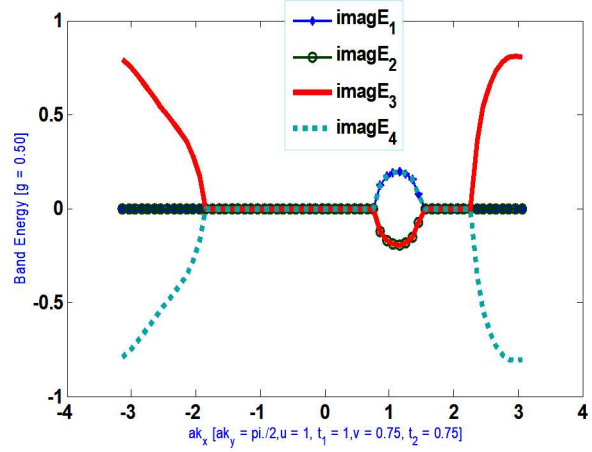
where $N_{j0} = [\psi_1^{j\dagger}(k)\psi_1^j(k) + \psi_2^{j\dagger}(k)\psi_2^j(k) + \psi_3^{j\dagger}(k)\psi_3^j(k) + \psi_4^{j\dagger}(k)\psi_4^j(k)]$ and $k = (k_x, k_y)$. As will be seen below, other functions of interest to investigate the exceptional points are $N_1 = \sum_{j=1}^{j=4} [\psi_1^{j\dagger}(k)\psi_1^j(k)]$ and $N_2 = \sum_{j=1}^{j=4} [\psi_2^{j\dagger}(k)\psi_2^j(k)]$. The equations $N_1 = 0 = N_2$ are basically the property of the self-orthogonality $\langle u^{(j)}(k_x = k_{x0}, k_y = k_{y0}) | u^{(j)}(k_x = k_{x0}, k_y = k_{y0}) \rangle = 0$ alluded to above. The explicit expressions of $\psi_r^j(k)$ ($r = 1, 2, 3, 4$) are shown in the Appendix A. In Figure 2, we have plotted these energy eigenvalues as a function of ak_x with $ak_y = 0$. The parameter values in (a) ((b)) are $u = t_1 = 1, v = t_2 = 0.75, \mu = 0$, and $\gamma = 0.77(0.75)$. In Figure(c), however, $\gamma = 0.59$. Throughout the paper, we choose 'u' to be the unit of energy. The Hamiltonian $H_{SSH,2D}(\mathbf{k})$ is PT -symmetric (eigenvalues are real) if $u = t_1$ in a limited region of two-dimensional BZ. For $u \neq t_1$, the Hamiltonian has complex eigenvalues (see Figure 2e), and thus the system enters a broken PT -symmetric phase. In Figure 2(d) (and 2(f)), we have shown the 3D(contour) plot of $J(k_x, k_y)$ as a function of ak_x and ak_y in the PT -symmetric (PT -symmetry broken) phase. At $ak_x \approx \pm 2.2$ and $ak_y = 0$, we indeed obtain $J(k_x, k_y) = 0$ in the PT -symmetric case. In Figure 2(e), we have plotted the real and the imaginary parts of the energy eigenvalues as a function of ak_x with $ak_y = 0$. At $ak_x \approx \pm 1.7$ and $ak_y = 0$, we once again obtain $J(k_x, k_y) = 0$. This may be seen in Figure 2(f). The parameter values used in Figure 2(e) and 2(f) are $u = 1, t_1 = 0.8, v = 0.75, t_2 = 0.60, \mu = 0$, and $\gamma = 0.75$. Additionally, in Figures (g) and (h), we have shown the plots of the real and the imaginary parts of the energy eigenvalues E_j ($j = 1, 2, 3, 4$) as a function of ak_x with $ak_y = \frac{\pi}{2}$. The parameter values in (g) ((h)) are $u = t_1 = 1, v = t_2 = 0.75, \mu = 0$, and $\gamma = 0.50$. Our graphical representations in Figures 2 (a) – 2(c) show that tunable gain/loss parameter

(γ) transforms the system from an insulator to a conductor when its numerical value is decreased.



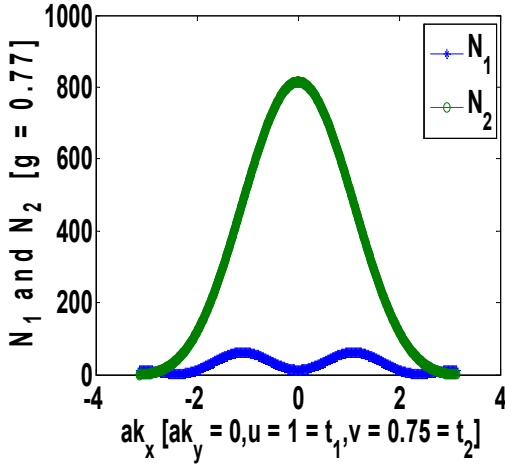


(g)

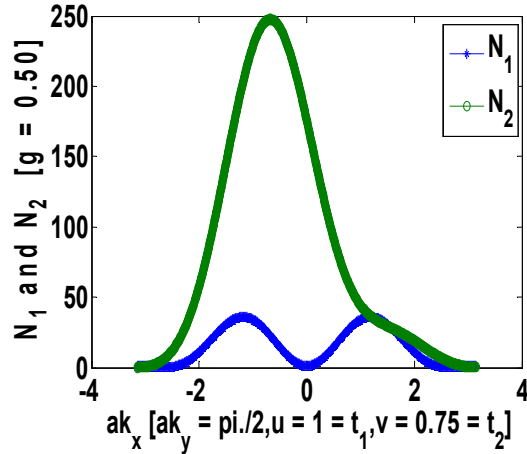


(h)

Figure 2. The plots of the energy eigenvalues E_j ($j = 1,2,3,4$) as a function of ak_x with $ak_y = 0$. The parameter values in (a) ((b)) are $u = t_1 = 1$, $v = t_2 = 0.75$, $\mu = 0$, and $\gamma = 0.77(0.75)$. In Figure(c), however, $\gamma = 0.59$. Here the symbol ‘g’ is the shorthand of ‘gamma(γ)’ in our 2DSSH model. The horizontal solid line represents the Fermi energy. (d) and (f) The 3D (contour) plot of $J(k_x, k_y)$ as a function of ak_x and ak_y in the PT – symmetric (PT – symmetry broken) phase. (e) The plots of the real and the imaginary parts of the energy eigenvalues as a function of ak_x with $ak_y = 0$. At $ak_x \approx \pm 1.7$ and $ak_y = 0$, we obtain $J(k_x, k_y) = 0$. This is indicated by horizontal and vertical solid lines in Figure 2(f). The parameter values used in Figure 2(e) and 2(f) are $u = 1$, $t_1 = 0.8$, $v = 0.75$, $t_2 = 0.60$, $\mu = 0$, and $\gamma = 0.75$. In Figures (e) and (f), we have shown the plots of the energy eigenvalues E_j ($j = 1,2,3,4$) as a function of ak_x with $ak_y = \frac{\pi}{2}$. The parameter values in (g) ((h)) are $u = t_1 = 1$, $v = t_2 = 0.75$, $\mu = 0$, and $\gamma = 0.50$.



(a)



(b)

Figure 3. The plots of $N_1 = \sum_{j=1}^4 [\psi_1^{j\dagger}(k)\psi_1^j(k)]$ and $N_2 = \sum_{j=1}^4 [\psi_2^{j\dagger}(k)\psi_2^j(k)]$ as a function of ak_x . In Figures 3(a), $\gamma = 0.77$, and $ak_y = 0$ and in 3(b) $\gamma = 0.50$, and $ak_y = \pi/2$. The other parameter values are the same as those in Figure 2(a).

In Figures 3 (a) ($\gamma = 0.77$, $ak_y = 0$) and 3(b) ($\gamma = 0.50$, $ak_y = \pi/2$), using the same parameter values as in 2(a), we have plotted $N_1 = \sum_{j=1}^{j=4} [\psi_1^{j\dagger}(k)\psi_1^j(k)]$ and $N_2 = \sum_{j=1}^{j=4} [\psi_2^{j\dagger}(k)\psi_2^j(k)]$ as a function of ak_x . We have already shown that at $ak_x \approx \pm 2.2$ and $ak_y = 0$, we indeed obtain $J(k_x, k_y) = 0$ in this PT -symmetric case. Figure 3(a) clearly indicates that these are exceptional points, for at these points the equation $N_1 = 0 = N_2$ is satisfied. However, as shown in Figure 3(b) which corresponds to PT -symmetry broken case (see also Figures 2(e) and 2(f)), this equation is not satisfied at the points $ak_x \approx \pm 1.7$ and $ak_y = 0$. We note in passing that in the non-Hermitian Hamiltonian case, perhaps the exceptional points can only occur if the Hamiltonian is PT -symmetric. We hasten to add that the verdict is not final on this issue as it requires a thorough investigation.

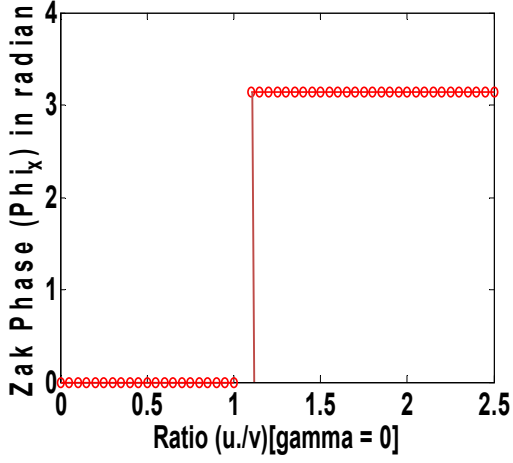
3. Zak Phase and Topoletric RLC Circuit

Zak Phase

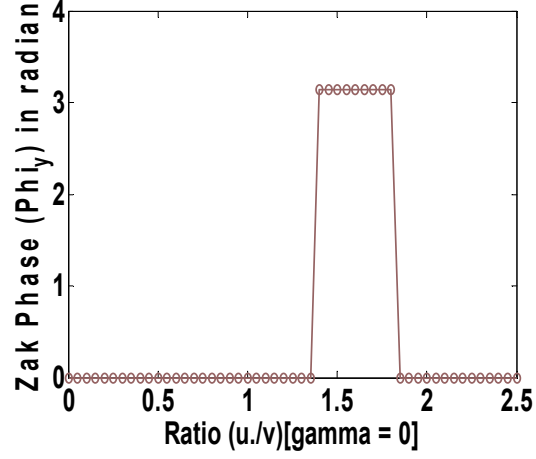
We have noted above that the Zak phase, which is essentially an integral in 1D, is defined as $\phi = \oint dk A(k)$ where $A(k)$ is the Berry connection. In 2D, we have the two components of the Zak phase, viz. $\{\phi_x(k_y), \phi_y(k_x)\}$. Furthermore, as shown in Figure 2, we have two bands corresponding to $j = 2, 4$ below the gap (which are needed to calculate $\{\phi_x(k_y), \phi_y(k_x)\}$) in the insulator state. These bands touch each other and then come apart as a parameter is varied. Since Berry curvature of such bands are additive [47], the Berry connection of the bands under consideration will be additive as well. We now consider the function $\phi_x(k_y)$ for which the Berry connection at $k_x = k_\alpha$ (where we have assumed $k_\alpha = \pi$ in our calculation and $\alpha = 1, \dots, N \gg 1$) and for the j^{th} band is given by $A^{(j)}(k_\alpha, k_y) = \langle u^{(j)}(k_\alpha, k_y) | i\partial_k | u^{(j)}(k_\alpha, k_y) \rangle$. Here $|u^{(j)}(k_\alpha, k_y)\rangle$ is the Bloch function and j now runs over all the bands below the band gap. The Zak phase for the j^{th} Bloch band $\phi_\alpha^{(j)}(k_y)$ in a small segment connecting k_α and $k_{\alpha+1}$ is $\phi_\alpha^{(j)}(k_y) = A^{(j)}(k_\alpha, k_y) \Delta(ak_\alpha) = i\langle u^{(j)}(k_\alpha, k_y) | u^{(j)}(k_{\alpha+1}, k_y) \rangle - i\langle u^{(j)}(k_\alpha, k_y) | u^{(j)}(k_\alpha, k_y) \rangle$. In our numerical calculation, we have assumed $\Delta(ak_\alpha) = \Delta(ak) \ll 1$. We have used Matlab package for the numerical calculation. It follows that $\langle u^{(j)}(k_\alpha, k_y) | u^{(j)}(k_{\alpha+1}, k_y) \rangle = 1 - i\phi_\alpha^{(j)}(k_y) \approx \exp(-i\phi_\alpha^{(j)}(k_y))$. In view of the Wilson loop approach [48,49], the total Zak phase $\phi_x(k_y)$ could be calculated by compounding the discrete Zak phase from each small segment $\Delta(ak_\alpha)$. We find $\exp(-i\phi_x(k_y)) = \prod_{\alpha=1}^{\alpha=N} \sum_{j=2,4} \langle u^{(j)}(k_\alpha, k_y) | u^{(j)}(k_{\alpha+1}, k_y) \rangle$ following refs. [47,50]. Upon using this expression, the Zak phase component ϕ_x could be written as

$$\phi_x = \left(\frac{1}{2\pi}\right) \int_{-\pi}^{+\pi} \text{Im}[\ln\{\prod_{\alpha=1}^{\alpha=N} \sum_{j=2,4} \langle u^{(j)}(k_\alpha, k_y) | u^{(j)}(k_{\alpha+1}, k_y) \rangle\}] dk_y \quad (11)$$

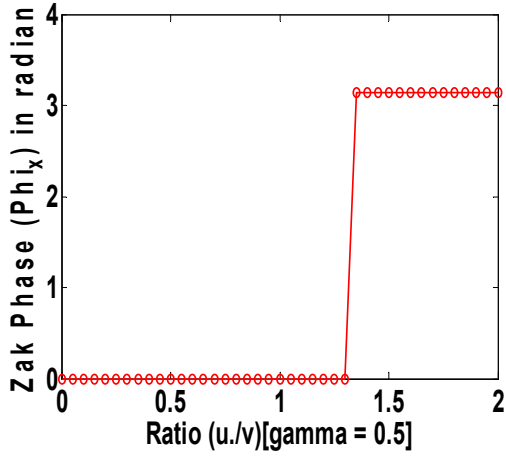
The other component of the vectored Zak phase, viz. ϕ_y , can be obtained in a similar manner. We have plotted the vectored Zak phase components ϕ_x and ϕ_y as a function of $\frac{u}{v}$ in Figures 4(a) – 4(d). The plots indicate that the conventional bulk-boundary correspondence depends crucially on the ratio $\frac{u}{v}$. In Figures 4(a) and 4(b), we have assumed $\gamma = 0$, whereas in 4(c) and 4(d) we have assumed $\gamma = 0.50$. In these figures, the hopping parameters $t_1 = u$ and $t_2 = v$. Furthermore, we note that, here ϕ_x and ϕ_y approximate $\pi = 4 \arctan(1) \approx 3.1416$ (correct to 4 decimal places) with relative error $\eta = 0.0021$.



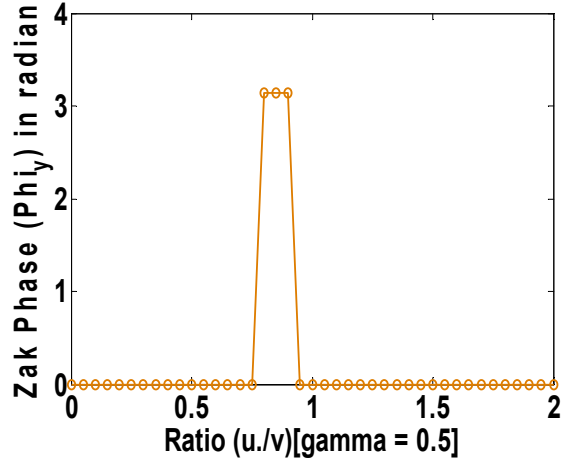
(a)



(b)



(c)



(d)

Figure 4. The plots of the vectored Zak phase components ϕ_x and ϕ_y as a function of $\frac{u}{v}$. In these figures, the hopping parameters $t_1 = u$ and $t_2 = v$. In Figures 4(a) and 4(b), we have assumed $\gamma = 0$, whereas in 4(c) and 4(d) we have assumed $\gamma = 0.50$.

Topoletric RLC Circuit

As regards the topoletric circuits, we may note that an LC system, where each unit cell consists of a pair of capacitors C_1 and C_2 with identical inductors L between them and an alternating driving voltage source with frequency ω , with periodic boundary conditions is described by the grounded Laplacian of the form $J_{SSH}(k_x) = i\omega \left(C_1 + C_2 - \frac{1}{\omega^2 L} \right) \sigma_0 - i\omega \left[(C_1 + C_2 \cos(ak_x)) \sigma_x + (C_2 \sin(ak_x)) \sigma_y \right]$ where σ_j 's are Pauli matrices. The Laplacian has total resemblance with the 1D-SSH model. This has been analyzed in detail in ref. [51]. Motivated by this work, we have carried out a preliminary investigation of a 2D topoletric circuit (in section 3) below.

The mapping of the current flow in a topoelectric circuits with a network of elements like resistors, inductors and capacitors, in a form similar to a tight-binding Hamiltonians of 1D/2D SSH model, is possible [51-55] where resistors (R), capacitances (C) and inductances (L) act as the hopping parameters. We consider below a topoelectric *RLC* circuit as shown in Figure 1. The resistors R (not shown) are assumed to be in parallel with the capacitors (C). This figure depicts nodal points with the voltages $V_1, V_2, V_3, \text{ and } V_4$ corresponding to the four nodes 1,2,3, and 4, respectively. Upon using Kirchoff's laws, the current flowing out of a node $j = 1,2,3,4$ could be written as $I_{N,j} = \sum_{k \neq j} Y_L (V_j - V_k) + Y_C V_j$ where $\sum_{k \neq j} Y_L (V_j - V_k)$ is equal to the current flowing out of the node j to other nodes k linked by admittance $Y_L = -\frac{i}{\omega L}$ and the current flowing to ground with admittance $Y_C = i\omega C + R^{-1}$. The driving voltage of the circuit may be assumed to have frequency ω . Upon using the formulation presented in references [51,54], we establish below link of with topological systems: In the case of lattice systems, the indexing of eigenmodes by momentum \mathbf{k} and band index α is possible using Bloch's theorem. Similarly, we write here for the eigenmode $\xi_{k,\alpha}(\mathbf{r}, \beta) = \zeta_\alpha(\mathbf{k}, \beta) \exp(i\mathbf{k} \cdot \mathbf{r})$, where a node (N, j) (may be referred to as a lattice site analogous to a lattice system) is indexed by its position \mathbf{r} and sublattice (if any) label β . The admittance between two sites $(\mathbf{0}, \beta)$ and (\mathbf{r}, β') takes the form $Y_r^{\beta\beta'} = \left\{ \sum_{k, \alpha} \frac{|\zeta_\alpha(\mathbf{k}, \beta) - \zeta_\alpha(\mathbf{k}, \beta') \exp(i\mathbf{k} \cdot \mathbf{r})|^2}{J_{k,\alpha}} \right\}^{-1}$. The inverse wavelenghts $\mathbf{k} = (k_x, k_y)$ take care of spatial modulation to the circuit elements in the two directions of the circuit and the $J_{k,\alpha}$ is circuit Laplacian matrix (\mathbf{J}) element to be introduced below for a RLC circuit. In fact, for such circuits, the voltage (V) and current (I) column vectors are related as $\mathbf{J} V = \lambda V = I$. Upon comparing this fundamental circuit equations with the Schrodinger Equation $H \psi = E \psi$, both in explicit matrix form, we notice that \mathbf{J} has a role similar to the Hamiltonian H . Thus, if the (dimensionless) admittance between two nodes $(\mathbf{0}, \beta)$ and (\mathbf{r}, β') becomes much less than one, there exist nontrivial eigenstates with the eigenvalues $\lambda \rightarrow 0$. This drastic increase of the impedance corresponds to the robust topological boundary resonance (TBR) condition in RLC circuits. The noting above provides us with a valuable insight that a formulation starting from circuit theory may allow us to have a sneak peek of unusual quantum phenomena.

One can write the current flowing out of the four nodes in Figure 1(b) in the explicit matrix form as $\mathbf{I} = i\omega \mathbf{J} \mathbf{V}$ where

$$\mathbf{J} = \begin{pmatrix} b & a_2 + a_1 \exp(-ik_x) & 0 & a_2 + a_1 \exp(-iak_y) \\ a_2 + a_1 \exp(ik_x) & b & a_2 + a_1 \exp(-ik_y) & 0 \\ 0 & a_2 + a_1 \exp(ik_y) & b & a_2 + a_1 \exp(-ik_x) \\ a_2 + a_1 \exp(ik_y) & 0 & a_2 + a_1 \exp(ik_x) & b \end{pmatrix} \quad (12)$$

A comparison shows that Eq. (12) has some degree of similarity with the 2D SSH model in Eq.(5). The column matrices \mathbf{I} and \mathbf{V} are given below:

$$\mathbf{I} = \begin{pmatrix} I_{N,1}(k_x, k_y) \\ I_{N,2}(k_x, k_y) \\ I_{N,3}(k_x, k_y) \\ I_{N,4}(k_x, k_y) \end{pmatrix}, \quad \mathbf{V} = \begin{pmatrix} V_1 \\ V_2 \\ V_3 \\ V_4 \end{pmatrix}, \quad a_1 = \frac{1}{\omega^2 L_1}, \quad a_2 = \frac{1}{\omega^2 L_2}, \quad b = \left(C - \frac{i}{R\omega} - 2a_1 - 2a_2 \right). \quad (13)$$

The eigenvalues λ of the circuit Laplacian matrix given above in (12) are obtained quite easily. The imaginary part of the secular equation yields $C - 2a_1 - 2a_2 = 0$. This gives $\omega = \sqrt{\frac{2}{(L_1+L_2)C}}$. For the parameter values $L_1 = 10 \text{ mH} = L_2$, and $C = 0.01 \mu\text{F}$, we obtain $\omega = 10^5 \text{ s}^{-1}$. The real part of equation, however, involves the inverse modulation wavelengths (k_x, k_y) . The real part yields

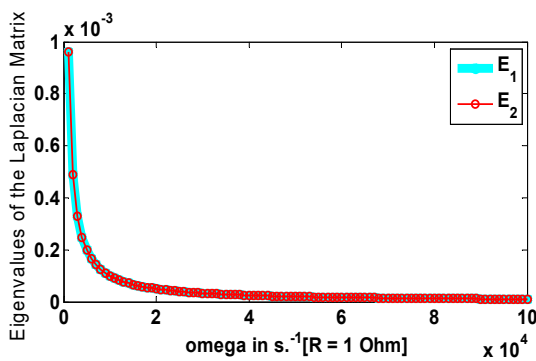
$$E(k_x, k_y) = C - 2a_1 - 2a_2 \pm \sqrt{\left(\frac{1}{(R\omega)^2} + P \pm \sqrt{P^2(k_x, k_y) - Q^2(k_x, k_y)}\right)}, \quad (14)$$

where

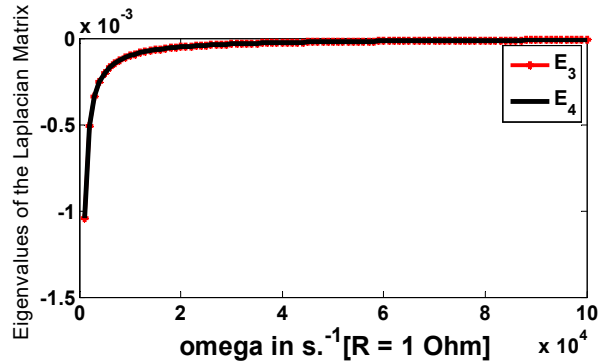
$$P(k_x, k_y) = 2a_1^2 + 2a_1a_2(\cos(k_x) + \cos(k_y)) + 2a_2^2, \\ Q^2(k_x, k_y) = \sum_{j=(x,y)} (2a_1^2 + 2a_1a_2\cos(k_j) + 2a_2^2)^2 - (a_1^2 + 2a_1a_2\cos(k_y) + a_2^2) \times \\ (2a_2^2 + 4a_1a_2\cos(k_x) + 2a_1^2\cos(2k_x)). \quad (15)$$

The plots of $E(k_x, k_y)$ as a function of ω , for the parameter values $L_1 = 0.1 \text{ mH} = L_2$, and $C = 0.01 \mu\text{F}$, are given below in Figure 5 for $R = (1, 26, 50) \text{ Ohm}$.

The plots in figure 5 show that the topological boundary resonance (TBR) condition $E = 0$ in RLC circuit is satisfied when $R \sim 1 \text{ Ohm}$ or less. The boundary resonance occurs at $\omega \sim 3 \times 10^4 \text{ s}^{-1}$ for all four eigenvalues obtained equating $\text{Real}(E)$ with zero. The value of the inverse wavelengths $\mathbf{k} = (k_x, k_y)$, which take care of spatial modulation to the circuit elements in the two directions of the circuit, have no significant influence on the value of ω . For higher resistances (as shown in Figures 5(c)-5(f)), (E_1, E_2) do not become zero. One may draw the conclusion that the compliance of the robust TBR condition is possible in a RLC topoelectric circuit when $R \leq 1 \text{ Ohm}$. In other words, a larger R does not favor TBR. It may be noted that the topological boundary resonances remain robust even in the face of significant nonuniformity of circuit elements [51], promising high-precision identification in a realistic measurement. With series resistance R on the inductor, one needs to replace the impedance of each inductor replaced by $i\omega L \rightarrow i\omega L + R$.



(a)



(b)

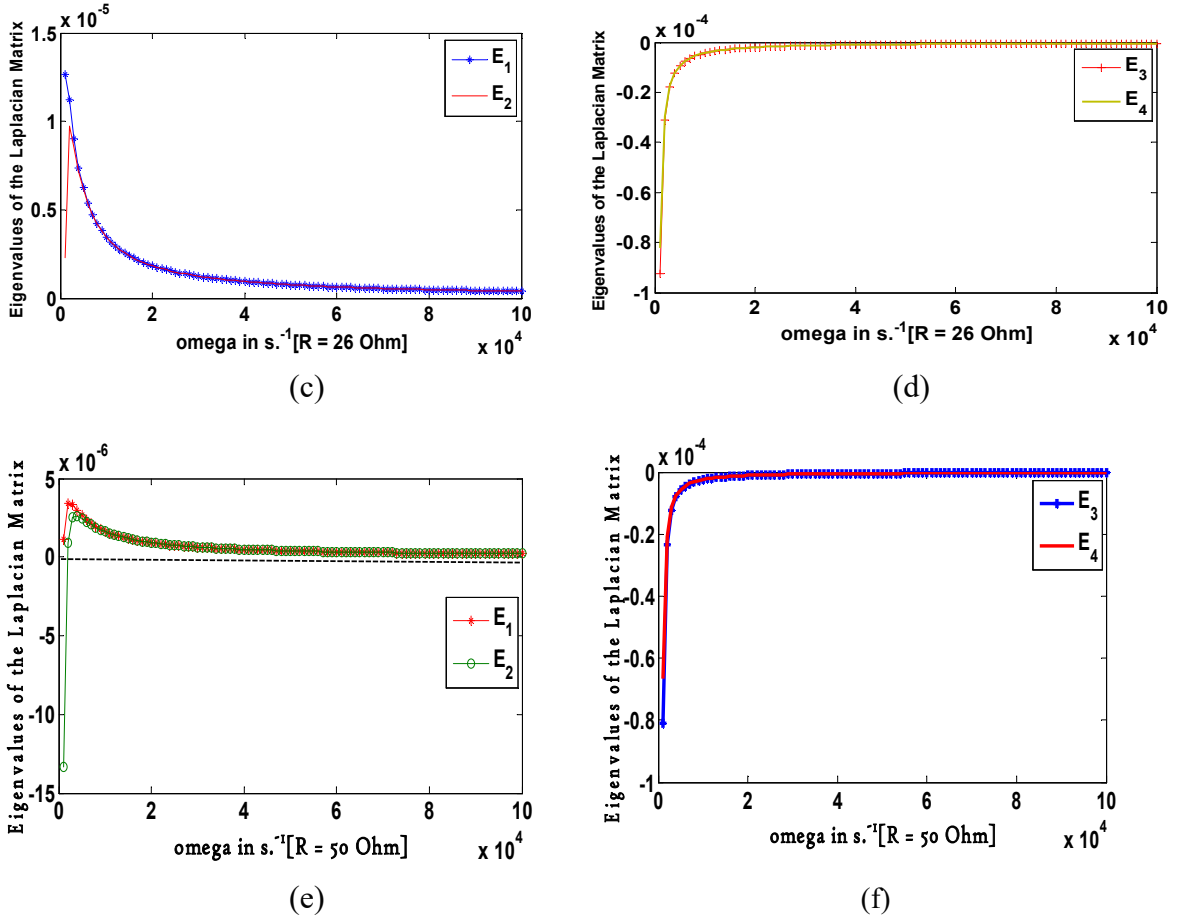


Figure 5. The plots of the real part of eigenvalues of the circuit Laplacian matrix in (12) as a function of ω in s^{-1} . The parameter values are $L_1 = 0.1 \text{ mH} = L_2$, $C = 0.01 \mu\text{F}$, and $R = (1, 26, 50) \text{ Ohm}$.

4. Staggered Hopping Amplitude ($v \neq t_2$)

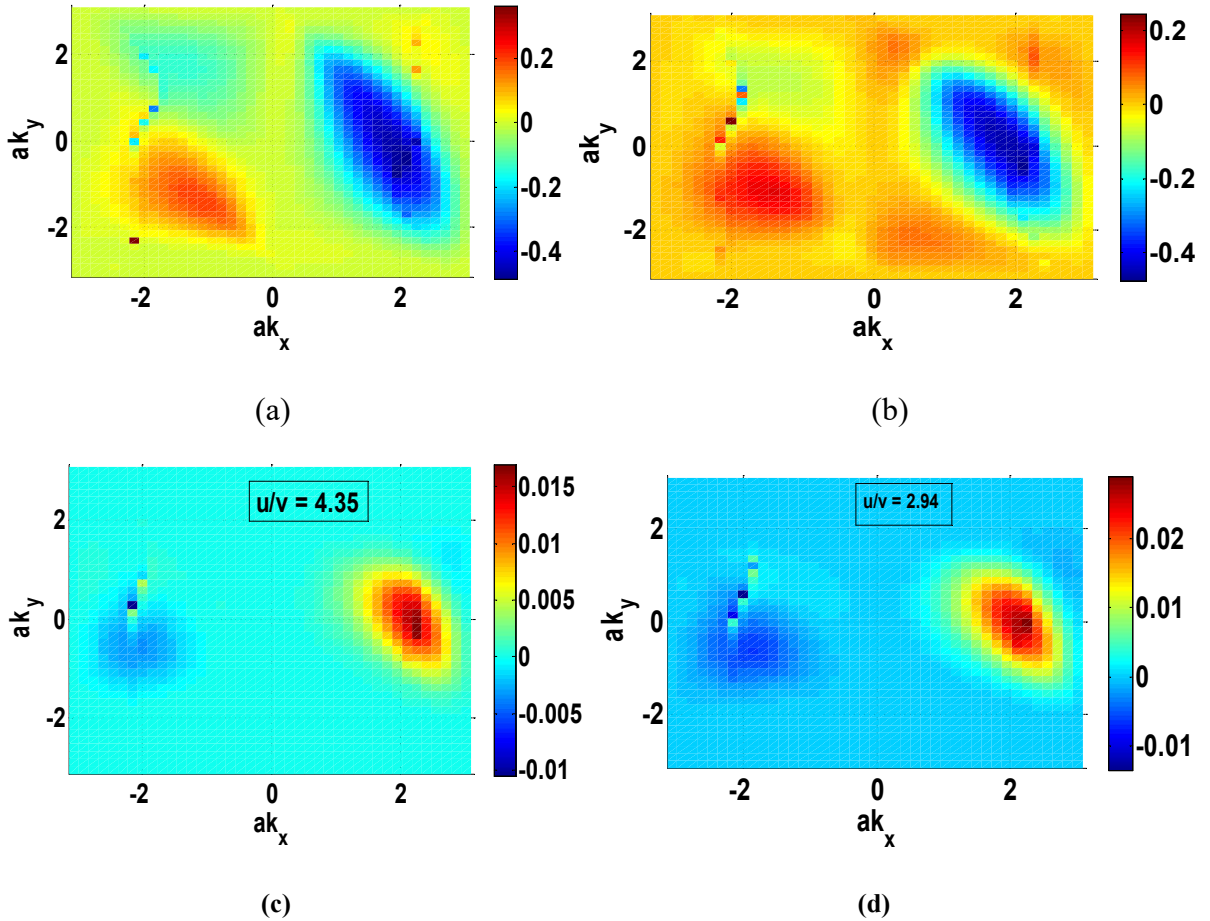
In this section, we consider a case where the hopping amplitudes are staggered ($v \neq t_2$) in the \hat{y} - direction. As mentioned in section 2, this leads the broken TRS. In general, this may transform a weak topological insulator to a Chern insulator. The Chern insulator is realized, even in the absence of an external magnetic field, in a 2D lattice model that describes quantized Hall plateaus with the magnitude of the Chern number C to be unity. In particular, if PHS is unbroken, the task of the analytical calculation of C , which otherwise is quite daunting, is somewhat manageable. It must be mentioned that, apart from broken TRS, an important requirement for obtaining the integer value of the chern number is that a band-gap, at the $\Gamma(0,0)$ point of the 2D BZ, between the bands closer to the Fermi energy must exist. If the gap does not exist, calculating C becomes meaningless. The PT symmetric situation depicted in Figures 2(a) and 2(b), although satisfy one of the important requirements mentioned above (viz., a band-gap between the bands closer to the Fermi energy under certain range of parameter values) for obtaining the quantization of anomalous conductance and anomalous Nernst response, but in this case TRS is unbroken. Without broken TRS, the anomalous Hall and Nernst conductivities are identically equal to zero. In fact, on the broken TR symmetric or the

broken space-inversion symmetric (SIS) systems the non-zero Berry curvature (BC) gives rise to an anomalous velocity. This velocity, in turn, gives rise to anomalous transport current and, thus, an intrinsic Hall conductivity.

As discussed in section 2, when $v \neq t_2$ the time reversal symmetry is broken. In what follows we show that BC is finite despite the fact that the present 2D SSH model describes spin-polarized electrons where two copies of it are needed when applying the model to a real physical system, and there is no spin-orbit interaction (SOI) to connect the two copies; SOI lies at the heart of the anomalous effects. We use the symbol $\Omega_\alpha^z(k)$ to denote the z -component of BC for the α^{th} occupied band. The curvature is given by the Kubo formula [56,57]

$$\Omega_\alpha^z(k_x, k_y) = -2 \left[\text{Im} \sum_{\beta \neq \alpha} (E_\alpha(k_x, k_y) - E_\beta(k_x, k_y))^{-2} \left\langle u^{(\alpha)}(k_x, k_y) \left| \frac{\partial H_{SSH,2D}(k_x, k_y)}{\partial k_x} \right| u^{(\beta)}(k_x, k_y) \right\rangle \right. \\ \left. \times \left\langle u^{(\beta)}(k_x, k_y) \left| \frac{\partial H_{SSH,2D}(k_x, k_y)}{\partial k_y} \right| u^{(\alpha)}(k_x, k_y) \right\rangle \right], \quad (16)$$

where the energy eigenvalues $E_\alpha(k_x, k_y)$ in (12) and the corresponding eigenstates (see Appendix A) are dependent on the same set of parameters. The calculation outline is given in Appendix B. In Figure 6(a) and 6(b), we have shown the plots of BC in the z -direction for the



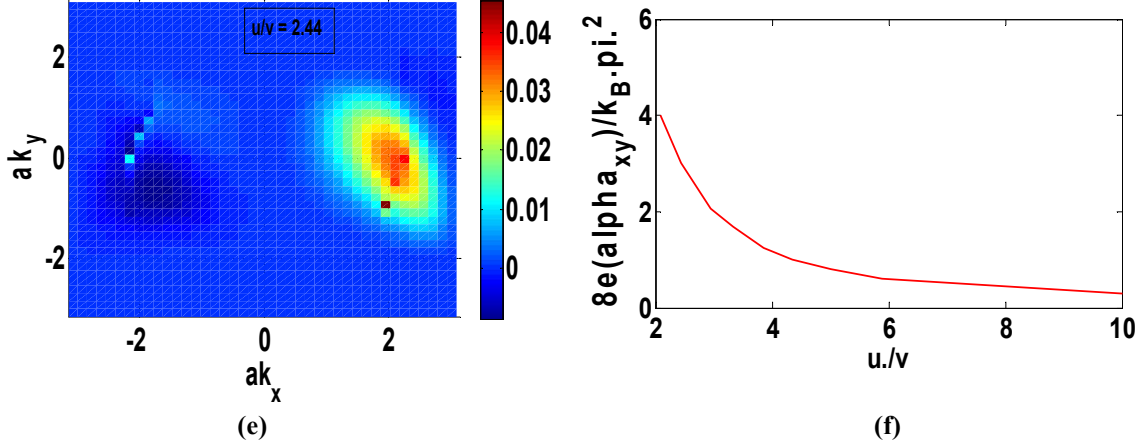


Figure 6. The plots of the Berry curvature in the z-direction as a function of (ak_x, ak_y) are shown in Figures (a) and (b). The numerical values of the parameters used in the plots are $u = t_1 = 1, t_2 = 0.5, v = 0.23$ (0.35), $\mu = 0$, and $\gamma = 0$.

staggered hopping amplitudes ($v \neq t_2$). The numerical values of the parameters used in the plots are $u = t_1 = 1, t_2 = 0.5, v = 0.23$ (0.35), $\mu = 0$, and $\gamma = 0$. The unavoidable feature of the Berry curvature (BC) calculation is that, though straightforward, but very lengthy.

In order to investigate Berry-phase effect in anomalous transport, we will first consider the anomalous Nernst conductivity (ANC) $\alpha_{xy}(\mu, T)$. The conductivity can be computed by integrating Berry curvature with entropy density over first BZ [58, 59]. In the low-temperature limit, upon using the Mott relation [58] we obtain

$$\alpha_{xy} \approx \frac{\pi^2 k_B^2 T}{3e} \sum_n \int d\mathbf{k} \Omega_{xy}^{(n)} \frac{\partial f(E_n(k))}{\partial E_n(k)}. \quad (17)$$

Here, μ is the chemical potential, and $f(\varepsilon)$ is the Fermi-Dirac distribution. At non-zero temperatures, however, the formula $\alpha_{xy}(\mu, T) = k_B \frac{e}{\hbar} \sum_n \int d\mathbf{k} \Omega_{xy}^{(n)} s(E_n(k))$ where the entropy density $s(E_n(k))$ is given by the expression $s(\varepsilon) = \frac{\varepsilon - \mu}{k_B T} f(\varepsilon) + \log\left(1 + \exp\left(\frac{\mu - \varepsilon}{k_B T}\right)\right)$, $f(\varepsilon) = \frac{1}{1 + \exp\left(\frac{\varepsilon - \mu}{k_B T}\right)}$ where k_B the Boltzmann constant. The integrand of the above

expression is contour plotted in Figure 6(c), 6(d) and 6(e) as a function of (ak_x, ak_y) for the different values of (u/v) as indicated in these figures. The numerical values of the parameters used in the plots are $u = t_1 = 1, t_2 = 0.5, \mu = 0$, and $\gamma = 0$. The Nernst conductivity α_{xy} is plotted as a function of (u/v) in Figure 6(f). The \mathbf{k} -integration is performed using the Matlab package. We make the problem of the integration manageable by breaking \mathbf{k} -space into small grids and carry on with the integration. Our approximations gets better when we add more grids. The plot in 6(f) shows that, as the ratio (u/v) increases, the Nernst response goes on decreasing.

The expression of the anomalous Hall conductance (AHC) is $\sigma_{AH} = \left(\frac{e^2}{h}\right) \sum_{\alpha \in \text{occupied bands}} \int_{BZ} \frac{d^2 k}{(2\pi)^3} f(E_\alpha(k) - \mu) \Omega_\alpha^z(k)$ where $f(E_\alpha(k) - \mu)$ is the fermion

occupation probability of the band $E_\alpha(k)$. Without sidestepping the issue of AHC, we also obtain σ_{AH} . It is usually difficult to exactly perform the integration of BC. So, we are forced to rely on the Matlab package, as mentioned above, to obtain approximate value of σ_{AH} . We obtain $\sigma_{AH} \approx 0.1 \left(\frac{e^2}{h}\right)$ with the appropriate choice of the parameter values and the number of grids. Therefore, the broken time reversal symmetry (expectedly leading to the possibility of the quantum anomalous Hall (QAH) effect) notwithstanding, we notice that the Chern number quantization ($\sigma_{AH} = C \left(\frac{e^2}{h}\right)$ where $C = \int_{\text{BZ}} \Omega_\alpha^z(k) \frac{d^2k}{(2\pi)^2}$ is the Chern number (an integer) - a topological invariant) may not be possible here.

5. Concluding remarks

In this paper, our focus was on a 2D non-Hermitian variant of SSH model. The Zak phase, we have calculated in section 3, is a quintessentially geometric object insensitive to the choice of gauge and unit cell origin. In our case of the 2D system with unbroken inversion symmetry, it is found that the vectored Zak phase components, acting as a topological index characterizing the bands, can either be equal to 0 or π . An explicit calculation of this geometric phase is demonstrated for our 2D SSH model. The values calculated and represented in Figure 3 predict the presence/absence of the gapless edge states. We hasten to add that the inversion symmetry protected quantized Zak phase only cannot establish the bulk-boundary correspondence as edge states may disappear in the topological nontrivial phase even in Hermitian systems [60-62]. This leads to the breakdown of the conventional bulk-boundary correspondence. Furthermore, when the dimensionless complex on-site potential magnitude and the hopping amplitudes become close to unity, exceptional points occur leading to the coalescence of eigenvalues and nontrivial eigenvector degeneracies. As regards the topoletric RLC circuit, we have found that that the compliance of the robust TBR condition is possible in our RLC topoletric circuit when $R \leq 1 \text{ Ohm}$. In other words, a larger R does not favor TBR. We have also made an attempt to calculate some topological properties of the model in section 4 despite the fact that an analytic calculation of topological properties is usually a daunting task. We find that the staggered hopping amplitude ($v \neq t_2$) leads to broken TRS with non-zero BC which in turn leads to finite anomalous Nernst conductivity. We, however, found that the Chern number quantization is not possible. These are the highlights of the present work.

The non-Hermitian systems possess an important property, viz. the localization of bulk modes at the boundaries [12-23]. This is referred to as the non-Hermitian skin effect (NHSE). The skin effect, that is bulk modes collapsing into boundary modes, is a key phenomenon in topological non-Hermitian systems. This has been predominantly studied in spinless systems. The NHSE originates from the intrinsic point gap topology of complex energy eigenvalues. Our future goal is to study this phenomenon extensively for the model given in Eq.(5). It is hoped that this will bring to light a new horizon in the study of non-Hermitian physics and the design of non-Hermitian systems.

References:

1. X. L. Qi and S. C. Zhang, Topological insulators and superconductors, Rev Mod Phys 83 (2011).

2. M. Sato and Y. Ando, Topological superconductors: a review, *Rep Prog Phys* 80 (2017).
3. M. Z. Hasan and C. L. Kane, Colloquium: Topological insulators, *Rev Mod Phys* 82, 3045 (2010).
4. Z. Song, Z. Fang, and C. Fang, (d−2)-dimensional edge states of rotation symmetry protected topological states, *Phys Rev Lett* 119 (2017).
5. T. Kawarabayashi and Y. Hatsugai, Bulk-edge correspondence with generalized chiral symmetry, arXiv: 2011.09164 v3(cond-mat. str-el)(2021).
6. A. Alase, S. Karuvade, and C. M. Scandolo, arXiv:2202.03864 v3[quant-ph](2022).
7. J. Zak. *Phys. Rev. Lett.*, 62 27472750 (1989).
8. P. Delplace, D. Ullmo, and G. Montambaux. *Phys. Rev. B*, 84 195452(2011).
9. W.P. Su, J.R. Schrieffer, A. J. and Heeger, *Phys. Rev. Lett.* 42, 1698 (1979).
10. S. H. Liu, W.L. Gao, Q. Zhang, *et al.* Topologically protected edge state in two-dimensional Su–Schrieffer–Heeger Circuit[J]. *Research*, 2019: 8609875 (2019).
11. F. Liu, *Phys. Rev. B* 108, 245140 (2023). This study explores the relationship between the n D SSH model and its (n−1)-D counterpart, identifying a hierarchical structure in the Hamiltonian that allows us to solve an arbitrary n D SSH model analytically.
12. N. Okuma, K. Kawabata, K. Shiozaki, and M. Sato, Topological Origin of Non-Hermitian Skin Effects, *Phys. Rev. Lett.* 124, 086801 (2020).
13. K. Kawabata, N. Okuma, and M. Sato, Non-Bloch band theory of non-Hermitian Hamiltonians in the symplectic class, *Phys. Rev. B* 101, 195147 (2020).
14. X. Zhang, T. Zhang, M.-H. Lu, and Y.-F. Chen, A review on non-Hermitian skin effect, *Adv. Phys.: X* 7, 2109431 (2022).
15. H. Gao, H. Xue, Z. Gu, T. Li, J. Zhu, and B. Zhang, Non-Hermitian route to higher-order topology in an acoustic crystal, arXiv:2007.01041 v1[cond-mat. mes-hall](2020).
16. S. Yao and Z. Wang, Edge States and Topological Invariants of Non-Hermitian Systems, *Phys. Rev. Lett.* 121, 086803 (2018).
17. S. Yao, F. Song, and Z. Wang, Non-Hermitian Chern Bands, *Phys. Rev. Lett.* 121, 136802 (2018). 13. F. K. Kunst, E. Edvardsson, J. C. Budich, and E. J. Bergholtz, Biorthogonal Bulk-Boundary Correspondence in Non-Hermitian Systems, *Phys. Rev. Lett.* 121, 026808 (2018).
18. K. Yokomizo and S. Murakami, Non-Bloch Band Theory of Non-Hermitian Systems, *Phys. Rev. Lett.* 123, 066404 (2019).
19. Y. Yi and Z. Yang, Non-Hermitian Skin Modes Induced by On-Site Dissipations and Chiral Tunneling Effect, *Phys. Rev. Lett.* 125, 186802 (2020).
20. Z. Yang, K. Zhang, C. Fang, and J. Hu, Non-Hermitian Bulk-Boundary Correspondence and Auxiliary Generalized Brillouin Zone Theory, *Phys. Rev. Lett.* 125, 226402 (2020).
21. V. M. Alvarez, J. B. Vargas, and L. F. Torres, Non-Hermitian robust edge states in one dimension: Anomalous localization and eigenspace condensation at exceptional points, *Phys. Rev. B* 97, 121401 (2018).

22. K. Zhang, Z. Yang, and C. Fang, Correspondence between Winding Numbers and Skin Modes in Non-Hermitian Systems, *Phys. Rev. Lett.* 125, 126402 (2020).
23. A. Ghatak, M. Brandenbourger, J. van Wezel, and C. Coullais, Observation of non-Hermitian topology and its bulk–edge correspondence in an active mechanical metamaterial, *Proc. Natl. Acad. Sci. U.S.A.* 117, 29561 (2020).
24. L. Xiao, T. Deng, K. Wang, G. Zhu, Z. Wang, W. Yi, and P. Xue, Non-Hermitian bulk–boundary correspondence in quantum dynamics, *Nat. Phys.* 16, 761 (2020).
25. D. Zou, T. Chen, W. He, J. Bao, C. H. Lee, H. Sun, and X. Zhang, Observation of hybrid higher-order skin topological effect in non-Hermitian topoelectrical circuits, *Nat. Commun.* 12, 7201 (2021).
26. Q. Zhou, J. Wu, Z. Pu, J. Lu, X. Huang, W. Deng, M. Ke, and Z. Liu, Observation of geometry-dependent skin effect in non-Hermitian phononic crystals with exceptional points, *Nat. Commun.* 14, 4569 (2023).
27. Q. Liang, D. Xie, Z. Dong, H. Li, H. Li, B. Gadway, W. Yi, and B. Yan, Dynamic Signatures of Non-Hermitian Skin Effect and Topology in Ultracold Atoms, *Phys. Rev. Lett.* 129, 070401 (2022).
28. L. Xiong, Q. Zhang, X. Feng, Y. Leng, M. Pi, S. Tong, and C. Qiu, Tracking Intrinsic Non-Hermitian Skin Effect in Lossy Lattices, *arXiv:2312.11490* (2023).
29. T. Hofmann, T. Helbig, F. Schindler, N. Salgo, M. Brzezińska, M. Greiter, T. Kiessling, D. Wolf, A. Vollhardt, A. Kabašić, et al., Reciprocal skin effect and its realization in a topoelectrical circuit, *Phys. Rev. Res.* 2, 023265 (2020).
30. L. Zhang, Y. Yang, Y. Ge, Y.-J. Guan, Q. Chen, Q. Yan, F. Chen, R. Xi, Y. Li, D. Jia, S.-Q. Yuan, H.-X. Sun, H. Chen, and B. Zhang, Acoustic non-Hermitian skin effect from twisted winding topology, *Nat. Commun.* 12, 6297 (2021).
31. Q. Zhang, Y. Leng, L. Xiong, Y. Li, K. Zhang, L. Qi, and C. Qiu, Construction and Observation of Flexibly Controllable High-Dimensional Non-Hermitian Skin Effects, *Adv. Mater.*, 2403108 (2024).
32. J. C. Budich and E. J. Bergholtz, Non-Hermitian Topological Sensors, *Phys. Rev. Lett.* 125, 180403 (2020).
33. H. Yuan, W. Zhang, Z. Zhou, W. Wang, N. Pan, Y. Feng, H. Sun, and X. Zhang, Non-Hermitian Topoelectrical Circuit Sensor with High Sensitivity, *Adv. Sci.* 10, 2301128 (2023).
34. C. H. Lee and S. Longhi, Ultrafast and anharmonic Rabi oscillations between non-Bloch bands, *Commun. Phys.* 3, 147 (2020).
35. W.-T. Xue, Y.-M. Hu, F. Song, and Z. Wang, Non-Hermitian Edge Burst, *Phys. Rev. Lett.* 128, 120401 (2022).
36. S. Weidemann, M. Kremer, T. Helbig, T. Hofmann, A. Stegmaier, M. Greiter, R. Thomale, and A. Szameit, Topological funneling of light, *Science* 368, 311 (2020).
37. A. McDonald and A. A. Clerk, Exponentially-enhanced quantum sensing with non-Hermitian lattice dynamics, *Nat. Commun.* 11, 5382 (2020).
38. S. Weidemann, M. Kremer, *et al.*, *Science*, Vol.368, issue 6488, 311(2020).
39. T. Yoshida, R. Peters, N. Kawakami, and Y. Hatsugai, *Progress of Theoretical and Experimental Physics* 2020, 12A109 (2020).
40. J. L. K. König, K. Yang, J. C. Budich, and E. J. Bergholtz, *Phys. Rev. Res.* 5, L042010 (2023).
41. H. Shen and L. Fu, *Phys. Rev. Lett.* 121, 026403 (2018).

42. J. C. Budich, J. Carlström, F. K. Kunst, and E. J. Bergholtz, *Phys. Rev. B* **99**, 041406 (2019).
43. K. Kawabata, T. Bessho, and M. Sato, *Phys. Rev. Lett.* **123**, 066405 (2019).
44. T. Yoshida, R. Peters, N. Kawakami, and Y. Hatsugai, *Phys. Rev. B* **99**, 121101 (2019).
45. E. Narevicius, P. Serra, and N. Moiseyev, *Europhys. Lett.* **62**, 789 (2003).
46. N. Moiseyev, *Non-Hermitian Quantum Mechanics* (Cambridge University Press) (2011).
47. J. E. Avron, R. Seiler, and B. Simon, *Phys. Rev. Lett.* **51**, 51 (1983).
48. K.G.Wilson, *Phys. Rev. D* **10**, 2445 (1974).
49. H. Wang, X. Tang, H. Xu, *et al. npj Quantum Mater.* **7**, 61 (2022).
50. M. Kim, and J. Rho, *Nanophotonics*, vol. 9, no. 10, 3227(2020).
51. C.H.Lee, S.Imhof, C. Berger, *et al. Commun Phys* **1**, 39 (2018).
52. R. Yang Qi Xun, *Molecular Frontiers Journal*, 04(Supp01) 9 (2020).
53. A. Blais, A. L. Grimsmo, S. M. Girvin, and A. Wallraff, *Rev. Mod. Phys.*, **93** 025005, (2021).
54. J. Dong, V. Juričić, and B. Roy, *Phys. Rev. Res.*, **3** 023056 (2021).
55. J. C. Perez-Pedraza, and J. E. Barrios-Vargas, arXiv:2402.05261v1 [cond-mat.mtrl-sci] (2024).
56. F. D. M. Haldane, *Phys. Rev. Lett.* **93**, 206602(2004).
57. M. Chen and S. Wan, *J. Phys. Condens. Matter* **24**, 325502 (2012).
58. D. Xiao, Y. Yao, Z. Fang, and Q. Niu, *Phys.Rev. Lett.* **97**, 026603 (2006).
59. D. Xiao, M.-C. Chang, Q. Niu, *Rev. Mod. Phys.* **82**, 1959-2007 (2010).
60. J.K. Asboth, L. Orozslány, and A. Pályi, *A short course on topological insulators*, *Lect. Notes Phys.* **919**, 1 (2016).
61. T.L. Hughes, E. Prodan, and B. A. Bernevig, *Phys. Rev. B* **83**, 245132 (2011).
62. G. van Miert, C. Ortix and C. Morais Smith, *2D Mater.* **4**, 015023 (2017).

Appendix A

The eigenstates $|u^{(\alpha)}(k)\rangle$ linked to the energy eigenvalues above could be written as $|u^{(\alpha)}(k)\rangle = N_{\alpha}^{-\frac{1}{2}}\phi_{\alpha}(k)$, where

$$N_{\alpha}(k) = \left[\left| \Delta_{10}^{(\alpha)}(k) \right|^2 + \left| \Delta_{11}^{(\alpha)}(k) \right|^2 + \left| \Delta_{20}^{(\alpha)}(k) \right|^2 + \left| \Delta_{21}^{(\alpha)}(k) \right|^2 + \left| \Delta_{30}^{(\alpha)}(k) \right|^2 + \left| \Delta_{31}^{(\alpha)}(k) \right|^2 + \left| \Delta_{40}^{(\alpha)}(k) \right|^2 + \left| \Delta_{41}^{(\alpha)}(k) \right|^2 \right], \quad (\text{A.1})$$

and $\phi_\alpha(k)$ is the transpose of the row vector $(\psi_1^{(\alpha)}(k) \ \psi_2^{(\alpha)}(k) \ \psi_3^{(\alpha)}(k) \ \psi_4^{(\alpha)}(k))$, $\alpha = \{1,2,3,4\}$. The elements $\psi_j^{(\alpha)}(k)$ are given by $\psi_1^{(\alpha)}(k) = \Delta_{10}^{(\alpha)} + i\Delta_{11}^{(\alpha)}$, $\psi_2^{(\alpha)}(k) = \Delta_{20}^{(\alpha)} + i\Delta_{21}^{(\alpha)}$, $\psi_3^{(\alpha)}(k) = \Delta_{30}^{(\alpha)} + i\Delta_{31}^{(\alpha)}$, and $\psi_4^{(\alpha)}(k) = \Delta_{40}^{(\alpha)} + i\Delta_{41}^{(\alpha)}$, where for the α^{th} band

$$\Delta_{10}^{(\alpha)} = (uvt_1 + vt_1^2 \cos(ak_x)) + ut_1 t_2 \cos(ak_y) + t_2 t_1^2 \cos(ak_x + ak_y) + u^2 v \cos(ak_x) + uvt_1 \cos(2ak_x) + t_2 u^2 \cos(ak_x + ak_y) + ut_1 t_2 \cos(2ak_x + ak_y) - (t_2 + v \cos(ak_y)) \times \{E^{(\alpha)^2}(k) - \gamma^2 - |p|^2\}, \quad (\text{A.2})$$

$$\Delta_{11}^{(\alpha)} = (vt_1^2 \sin(ak_x)) + ut_1 t_2 \sin(ak_y) + t_2 t_1^2 \sin(ak_x + ak_y) + u^2 v \sin(ak_x) + uvt_1 \sin(2ak_x) + t_2 u^2 \sin(ak_x + ak_y) + ut_1 t_2 \sin(2ak_x + ak_y) - (v \sin(ak_y)) \times \{E^{(\alpha)^2}(k) - \gamma^2 - (v + t_2 \exp(iak_y))(v + t_2 \exp(-iak_y))\}, \quad (\text{A.3})$$

$$\Delta_{20}^{(\alpha)} = E^{(\alpha)}(k) \left\{ (v + t_2 \cos(ak_y)) (t_1 + u \cos(ak_x)) - u t_2 \sin(ak_x) \sin(ak_y) + (t_2 + v \cos(ak_y)) (u + t_1 \cos(ak_x)) - v t_1 \sin(ak_x) \sin(ak_y) \right\} + \gamma \{ t_2 \sin(ak_y) (t_1 + u \cos(ak_x)) + u \sin(ak_x) (v + t_2 \cos(ak_y)) - v \sin(ak_y) \times (u + t_1 \cos(ak_x)) - t_1 \sin(ak_x) (t_2 + v \cos(ak_y)) \}, \quad (\text{A.4})$$

$$\Delta_{21}^{(\alpha)} = E^{(\alpha)}(k) \left\{ (t_2 \sin(ak_y)) (t_1 + u \cos(ak_x)) + u \sin(ak_x) (v + t_2 \sin(ak_y)) + (v \sin(ak_y)) (u + t_1 \cos(ak_x)) - t_1 \sin(ak_x) (t_2 + v \cos(ak_y)) \right\} - \gamma \{ (v + t_2 \cos(ak_y)) (t_1 + u \cos(ak_x)) + u t_2 \sin(ak_x) \sin(ak_y) + (t_2 + v \cos(ak_y)) (u + t_1 \cos(ak_x)) - v t_1 \sin(ak_x) \sin(ak_y) \}, \quad (\text{A.5})$$

$$\Delta_{30}^{(\alpha)} = |s|^2 (v + t_2 \cos(ak_y)) - (E^{(\alpha)}(k)^2 - \gamma^2) (t_1 + u \cos(ak_x)) + (uvt_2 + uv^2 \cos(ak_y)) + ut_2^2 \cos(ak_y) + uvt_2 \cos(2ak_y) + t_1 t_2 v \cos(ak_x) + t_1 \times (t_2^2 + v^2) \cos(ak_x + ak_y) + t_1 t_2 v \cos(2ak_y + ak_x), \quad (\text{A.6})$$

$$\Delta_{31}^{(\alpha)} = -|s|^2 (t_2 \sin(ak_y)) + (E^{(\alpha)}(k)^2 - \gamma^2) (u \sin(ak_x)) - uv^2 \sin(ak_y) - ut_2^2 \sin(ak_y) - uvt_2 \sin(2ak_y) - t_1 t_2 v \sin(ak_x) - t_1 (t_2^2 + v^2) \sin(ak_x + ak_y) - t_1 t_2 v \sin(2ak_y + ak_x), \quad (\text{A.7})$$

$$\Delta_{40}^{(\alpha)} = (E^{(\alpha)}(k))^3 - E^{(\alpha)}(k) \gamma^2 - E^{(\alpha)}(k) |p|^2 - E^{(\alpha)}(k) |s|^2, \quad (\text{A.8})$$

$$\Delta_{41}^{(\alpha)} = \gamma^3 + \gamma |p|^2 + \gamma |s|^2 - \gamma E^{(\alpha)}(k)^2. \quad (\text{A.9})$$

Appendix B

As regards the Berry curvature, the z-component of BC (see Eq.(12)) may be written as $\Omega_{xy}(k) = -2 \sum_{\alpha} \text{Im} \left\langle \frac{\partial u^{(\alpha)}(k)}{\partial k_x} \left| \frac{\partial u^{(\alpha)}(k)}{\partial k_y} \right. \right\rangle$. This follows from the Heisenberg equation of motion is $i\hbar \frac{d\hat{x}}{dt} = [\hat{x}, \hat{H}]$. In view of this equation, we find that the identity

$$\hbar \langle u_{\alpha}(k') | \hat{v}_j | u_{\alpha}(k) \rangle = (E_{\alpha}(k') - E_{\alpha}(k)) \left\langle u_{\alpha}(k') \left| \frac{\partial}{\partial k_j} \right| u_{\alpha}(k) \right\rangle$$

is satisfied for a system in a periodic potential and its Bloch states as the eigenstates $|u_{\alpha}(k)\rangle$. Here the operator $\hbar^{-1} \frac{\partial H(k)}{\partial k_j} = \hat{v}_j$ represents the velocity in the $j = (x, y)$ direction. The z-component of BC may now be written in the form $\Omega_{xy}(k) = -2 \sum_{\alpha} \text{Im} \left\langle \frac{\partial u^{(\alpha)}(k)}{\partial k_x} \left| \frac{\partial u^{(\alpha)}(k)}{\partial k_y} \right. \right\rangle$ upon using the identity above. We use this formula to present the outline of the calculation of BC below.

It is not difficult to see that for the present problem the product

$$\left\langle \frac{\partial u^{(\alpha)}(k)}{\partial k_x} \left| \frac{\partial u^{(\alpha)}(k)}{\partial k_y} \right. \right\rangle = \sum_{j=1,2,3,4} [(P_{jx}^{(\alpha)} P_{jy}^{(\alpha)} + Q_{jx}^{(\alpha)} Q_{jy}^{(\alpha)}) + i(P_{jx}^{(\alpha)} Q_{jy}^{(\alpha)} - Q_{jx}^{(\alpha)} P_{jy}^{(\alpha)})], \quad (\text{A.10})$$

where

$$\begin{aligned} P_{jx}^{(\alpha)} &= -\left(\frac{1}{2}\right) N_{\alpha}^{-\frac{3}{2}} (\partial_x N_{\alpha}) \Delta_{j0}^{(\alpha)} + N_{\alpha}^{-\frac{1}{2}} (\partial_x \Delta_{j0}^{(\alpha)}), \quad Q_{jy}^{(\alpha)} = -\left(\frac{1}{2}\right) N_{\alpha}^{-\frac{3}{2}} (\partial_y N_{\alpha}) \Delta_{j1}^{(\alpha)} + N_{\alpha}^{-\frac{1}{2}} (\partial_y \Delta_{j1}^{(\alpha)}), \\ Q_{jx}^{(\alpha)} &= -\left(\frac{1}{2}\right) N_{\alpha}^{-\frac{3}{2}} (\partial_x N_{\alpha}) \Delta_{j1}^{(\alpha)} + N_{\alpha}^{-\frac{1}{2}} (\partial_x \Delta_{j1}^{(\alpha)}), \quad P_{jy}^{(\alpha)} = -\left(\frac{1}{2}\right) N_{\alpha}^{-\frac{3}{2}} (\partial_y N_{\alpha}) \Delta_{j0}^{(\alpha)} + N_{\alpha}^{-\frac{1}{2}} (\partial_y \Delta_{j0}^{(\alpha)}), \end{aligned} \quad (\text{A.11})$$

$$(\partial_{x/y} N_{\alpha}) = 2 \sum_{j=1,2,3,4} [\Delta_{j0}^{(\alpha)} (\partial_{x/y} \Delta_{j0}^{(\alpha)}) + \Delta_{j1}^{(\alpha)} (\partial_{x/y} \Delta_{j1}^{(\alpha)})]. \quad (\text{A.12})$$

The symbol ∂_x (∂_y) above stands for the differential coefficient $\frac{\partial}{\partial k_x}$ ($\frac{\partial}{\partial k_y}$). Now that we have calculated a formal expression for the BC of α band, what remains to be done is to calculate various derivatives in (32). This is an exceedingly lengthy but straightforward task.